Actin networks voltage circuits

Stefano Siccardi ⓘ and Andrew Adamatzky ⓘ

Unconventional Computing Laboratory, Department of Computer Science, University of the West of England, Bristol, United Kingdom

Jack Tuszyński ⓘ

Department of Oncology, University of Alberta, Edmonton, Canada AB T6G 1Z2
and DIMEAS, Politecnico di Torino, Corso Duca degli Abruzzi 24, 10129, TO, Turin, Italy

Florian Huber ⓘ

Netherlands eScience Center, Science Park 140, 1098 XG Amsterdam, The Netherlands

Jörg Schnauß ⓘ

Soft Matter Physics Division, Peter Debye Institute for Soft Matter Physics,
Faculty of Physics and Earth Science, Leipzig University, Germany
and Fraunhofer Institute for Cell Therapy and Immunology (IZI), DNA Nanodevices Group, Leipzig, Germany

Filaments of the cellular protein actin can form bundles, which can conduct ionic currents as well as mechanical and voltage solitons. These inherent properties can be utilized to generate computing circuits solely based on self-assembled actin bundle structures. Starting with experimentally observed networks of actin bundles, we model their network structure in terms of edges and nodes. We compute and discuss the main electrical parameters, considering the bundles as electrical wires with either low or high filament densities. A set of equations describing the network is solved with several initial conditions. Input voltages, which can be considered as information bits, are applied in a set of points and output voltages are computed in another set of positions. We consider both an idealized situation, where pointlike electrodes can be inserted in any points of the bundles and a more realistic case, where electrodes lay on a surface and have typical dimensions available in the industry. We find that in both cases such a system can implement the main logical gates and a finite state machine.

I. INTRODUCTION

Actin filaments (AFs) and tubulin microtubules (MTs) represent the key components of cytoskeleton networks [1]. They have been experimentally demonstrated and modeled as ionic wave conducting biowires [2–8], and predicted to support conformational solitons [9–11], as well as orientational transitions of dipole moments [12–14]. These propagating localizations could carry information and transform it when interacting with one another. Hence, these cytoskeleton networks could be used as nanoscale computing devices [15]. This idea dates back to an early concept of subcellular computing on cytoskeleton networks [16–18] and was later developed further in the context of information processing on actin-tubulin networks of neuron dendrites [19]. When immersed in an ion-rich liquid environment, AFs can be viewed as wires that can conduct electrical currents [3,20]. Previously we have demonstrated computationally that these electrical currents can be used to implement Boolean gates [21]. A single AF hence can be conceived as a computing device in computational experiments. Its practical implementation under laboratory conditions, however, would be very challenging and likely beyond current technological possibilities. For this reason, we decided to adapt our computing schemes to more realistic scenarios of bundles of AFs instead of single AF units [22–24]. We developed a model of an actin droplet computer, where information is represented by traveling spikes of excitation and logical operations are implemented at the junctions of AF bundles [25–27]. The model developed treats the actin network as a continuum with propagating abstract excitation waves—modeled with FitzHugh-Nagumo equations. The model might be phenomenologically correct, but is not able to sufficiently describe the physics of the waves in the AF networks. Therefore we here propose a model more solidly rooted in the underlying physics. We consider the AF networks to be made of wires and their bundles to be connected at node locations. Each bundle has its own set of electrical parameters and facilitates the movement of ions along its length.

II. THE MODEL

A detailed description of key models that we used as foundation in this study can be found in [3], which was aiming at a description of AFs and contains the derivation of all the formulas. Let us highlight the assumptions on which the model was build. Each monomer in the filament has 11 negative excess charges. The double helical structure of the filament provides regions of uneven charge distribution such that pockets of higher and lower charge density exist. There is a well-defined distance, the so-called Bjerrum length λ_B, beyond which thermal fluctuations are stronger than the

electrostatic attraction or repulsion between charges in solution. It is inversely proportional to temperature and directly proportional to the ions' valence z:

$$\lambda_B = \frac{ze^2}{4\pi \epsilon \epsilon_0 k_B T},\tag{1}$$

where e is the electronic charge, ϵ_0 is the permittivity of the vacuum, ϵ is the dielectric constant of the solution with AFs immersed in (estimated to be similar to $\epsilon_{\text{water}} \approx 80$), k_B is the Boltzmann's constant, and T is the absolute temperature. If δ is the mean distance between charges, counterion condensation is expected when $\lambda_B/\delta > 1$. Considering the temperature is $T = 293$ K and the ions are monovalent, [3] finds $\lambda_B = 7.13 \times 10^{-10}$ m and [20] $\lambda_B = 13.8 \times 10^{-10}$ m for Ca^{2+} at $T = 310$ K. Considering actin *filaments*, δ is estimated to be 0.25 nm because assuming an average of 370 monomers per μm there are approximately $4e$/nm. Each monomer behaves like an electrical circuit with inductive, capacitive, and resistive components. The model is based on the transmission line analogy.

The capacitance C is computed considering the charges contained in the space between two concentric cylinders, the inner with radius half the width of a monomer ($r_{\text{actin}} = 2.5$ nm) and the outer with radius $r_{\text{actin}} + \lambda_B$; both cylinders are one monomer high (5.4 nm). Thus,

$$C_0 = \frac{2\pi \epsilon l}{\ln\left(\frac{r_{\text{actin}}+\lambda_B}{r_{\text{actin}}}\right)},\tag{2}$$

where $l \approx 5.4$ nm is the length of a monomer.

The charge on this capacitor is assumed to vary in a nonlinear way with voltage, according to the formula

$$Q_n = C_0\left(V_n - bV_n^2\right).\tag{3}$$

Nonlinear voltage dependence of electrochemical capacitance for nanoscale conductors is due to finite density of states of the conductors. Details can be found in [28,29]. We did not try to evaluate this parameter; instead, we used some trial values in our equations and found that, as long as b is reasonably small, the solutions converge to the constant ones in the cases that we considered. So we focused on constant solutions, and we can say that nonlinearity is not needed for our results.

The inductance L is computed as

$$L = \frac{\mu N^2 \pi (r_{\text{actin}} + \lambda_B)^2}{l},\tag{4}$$

where μ is the magnetic permeability of water and N is the number of turns of the coil, that is the number of windings of the distribution of ions around the filament. It is approximated by counting how many ions can be lined up along the length of a monomer as $N = l/r_h$, and it is supposed that the size of a typical ion is $r_h \approx 3.6 \times 10^{-10}$ m.

The resistance R is estimated considering the current between the two concentric cylinders, obtaining

$$R = \frac{\rho \ln[(r_{\text{actin}} + \lambda_B)/r_{\text{actin}}]}{2\pi l},\tag{5}$$

where resistivity ρ is approximately given by

$$\rho = \frac{1}{\Lambda_0^{K^+} c_{K^+} + \Lambda_0^{Na^+} c_{Na^+}}.\tag{6}$$
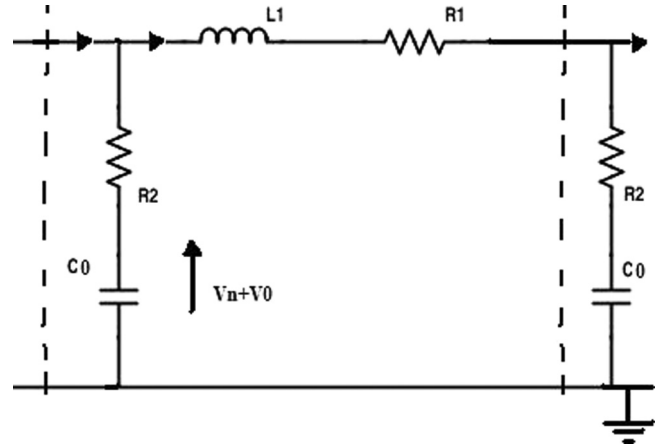

FIG. 1. A circuit diagram for the *n*th unit of an actin filament. From [3].

Here, c_{K^+} and c_{Na^+} are the concentrations of sodium and potassium ions, which were considered in previous papers to be 0.15 and 0.02 M, respectively; $\Lambda_0^{K^+} \approx 7.4\ (\Omega\,\text{m})^{-1}\,\text{M}^{-1}$ and $\Lambda_0^{Na^+} \approx 5.0\ (\Omega\,\text{m})^{-1}\,\text{M}^{-1}$ are positive constants that depend only on the type of salts but not on the concentration [3]. With this formula R_1 is computed and R_2 is taken as $1/7R_1$. Here R_1 accounts for viscosity.

Figure 1 illustrates the circuit schema, where an actin monomer unit in a filament is delimited by the dotted lines.

The main equation for filaments is the following, derived from [3] (see Fig. 1 for the meaning of R_1, etc.):

$$\begin{aligned}
LC_0 &\frac{d^2}{dt^2}\left(V_n - bV_n^2\right) \\
&= V_{n+1} + V_{n-1} - 2V_n - R_1 C_0 \frac{d}{dt}\left(V_n - bV_n^2\right) \\
&\quad - R_2 C_0 \left\{2\frac{d}{dt}\left(V_n - bV_n^2\right) - \frac{d}{dt}\left(V_{n+1} - bV_{n+1}^2\right)\right. \\
&\quad \left. - \frac{d}{dt}\left(V_{n-1} - bV_{n-1}^2\right)\right\}.
\end{aligned}\tag{7}$$

In [21] we used this equation to compute the evolution of some tens of monomers in a filament.

It must be observed that the Bjerrum length will probably not be constant, but may vary both from point to point and with time. Also, one could consider the effects described in [30] leading to charge density waves. However, the effects reported in that work refer mainly to electrostatically condensed bundles, while the bundles in our experimental setting were built using different network formation processes, that is via depletion forces. The depletion forces are a fundamental, entropic effect, which does not rely on counterion condensation [31,32]. Thus, the situations, i.e., the charge distributions, are completely different. Moreover, the present work is a computational analysis to prepare real experiments and to speculate about potential solutions, and will use the simplest possible stimuli, i.e., constant ones. Therefore we did not consider phenomena that, even if they happened, in this context might be considered transient.

TABLE I. C_0, L, and R_1 for high density bundles.

Width	200 nm	450 nm	700 nm
C_0 in pF	33.8×10^{-4}	76×10^{-4}	11.8×10^{-3}
L in pH	1668	8378	20227
R_1 in MΩ	0.173	0.077	0.049

TABLE II. C_0, L, and R_1 for low density bundles.

Filaments	1	25	50	75
C_0 in pF	102.6×10^{-6}	4.1×10^{-6}	2×10^{-6}	1.4×10^{-6}
L in pH	1.92	7.66×10^{-2}	3.83×10^{-2}	2.56×10^{-2}
R_1 in MΩ	5.7	0.23	0.11	0.08

III. EXTENSION TO BUNDLE NETWORKS

In order to extend the model to bundle networks, we must compute the suitable electrical parameters. The actin filaments are made of elements, the actin monomers. We will model bundles as made of elements of the same height of a single monomer, and width depending on the bundle density. We will consider two possibilities:

(1) The filament density in the bundle is so low that each filament stands at a distance greater than twice λ_B from all the others. In this situation, we assume that filaments do not interact and that each one behaves as if it would not be in the bundle.

(2) The inner-bundle density is high enough that areas closer than λ_B to the filaments intersect. In this situation, we will conservatively assume that the influences of the filaments' ions cancel out.

In case 1 we can either consider the parameters for a filament and solely multiply results by the number of filaments in the bundle or compute C, L, and R using the standard formulas for electrical parallel circuits. In case 2 we only use the bundle radius instead of the filament one in the above formulas.

Considering a Bjerrum length $\lambda_B = 7.13 \times 10^{-10}$ m [3], results for high density bundles at different bundle widths are displayed in Table I. Results for low density bundles made of varying filament numbers are shown in Table II.

In the following we will define equations for nodes. Equation (7) applies to elements *inside* the bundle, so we will use Eq. (8) instead, where n is the index of the element, M is the number of elements linked to it, and the suffix n_k ranges in the set of such linked elements.

The term F_n represents an input voltage, which is supposed to be nonzero only for some values of n:

$$\frac{d^2}{dt^2}\left(V_n - bV_n^2\right)$$
$$= \frac{1}{LC_0}\left\{\sum_{k=1}^{M} V_{n_k} - M \times V_n + F_n - R_1 C_0 \frac{d}{dt}\left(V_n - bV_n^2\right)\right.$$
$$\left. - R_2 C_0 \left\{M \times \frac{d}{dt}\left(V_n - bV_n^2\right) - \sum_{k=1}^{M} \frac{d}{dt}\left(V_{n_k} - bV_{n_k}^2\right)\right\}\right\}.$$
$$(8)$$

These equations can represent any type of element in the network. When $M = 2$, they coincide with (7) and represent internal elements of a bundle. When $M = 1$, they refer to a free terminal element of a bundle that is not connected to anything else. We note that in [21] we used a slightly different equation for this case, namely we always kept $M = 2$.

The present form is more consistent with the model and its generalization. Other values of M represent generic nodes.

IV. THE NETWORK

We used a stack of low-dimensional images of the three-dimensional actin network, produced in experiments on the formation of regularly spaced bundle networks from homogeneous filament solutions [27]. The network was chosen because it resulted from a protocol that reliably produces regularly spaced networks due to self-assembly effects [27,33] and thus could be used in prototyping of cytoskeleton computers. From the stack of images we extracted a network description, in terms of edges and nodes, and used it as a substrate to compute the electrical behavior. The extracted structure takes into account the main bundles in each image, with their intersections, and an estimate of bundles that can connect nodes in two adjacent images. It is not an accurate portrait of all the bundles, but it captures the main characteristics of the network.

The main steps to compute the network structure were:

(1) After some preprocessing of the images (e.g., thresholding, contour finding, distance transform, etc.), we looked at the points placed at the local maxima of distance from background. We considered that these are the nodes of the network. Each node found in this way has a center and a radius (corresponding to the circle that can be inscribed in the foreground).

(2) We then tried to link nodes to each other with straight lines or elliptical arcs, checking that they do not go out of the bundles (with some tolerance, as the bundles are often bent). For this, starting from, e.g., node 1, we considered the point spaced about 16 pixels along the line from node 1 to, e.g., node 2. If its color was above the threshold, we went on to the next point 16 pixel farther. If not, we considered the points in a neighborhood 4 pixel wide: if at least one was above the threshold, we considered that the edge is still in the bundle and went on, if not we stopped.

(3) If we could not find any straight line, we tried some elliptical arcs, with big axis = distance between nodes and a range of small axes, using the same procedure

(4) When we were able to reach, e.g., node 2 from node 1, we added the edge to the network, with its length (distance of the linked nodes for straight edges or approximate ellipse arc length for the others) and width = the average of the radii of its nodes; when we were not able to reach node 2 we did not add the edge; if a node was not connected to anything we did not consider it anymore.

(5) We also tried to detect edges between images. For this, we merged the bundles of two consecutive ones, shrunk them a bit, and applied the method of step 2 to link nodes. We used a lower tolerance in this step and considered straight lines only.

TABLE III. Parameters of the actin network used in the modeling.

Parameter	Value
Number of nodes in the main connected graph	2968
Number of edges in the main connected graph	7583
Max number of nodes linked to a node	13
Average number of nodes linked to a node	5.07
Standard deviation of nodes linked to a node	2.14
Average radius of edges in pixels	8.48
Max radius of edge in pixels	20
Min radius of edge in pixels	3
Standard deviation of radii of edges in pixels	2.62
Average edge radius, one pixel is 244.14 nm	2.07 μm
Average length of edges in pixels	70.11
Max length of edge in pixels	465.40
Min length of edge in pixels	4.12
Standard deviation of lengths of edges in pixels	41.54
Average edge length, one pixel is 244.14 nm	17.12 μm

All computations described here and in the other sections were performed using Python including its libraries Matplotlib [34] and Scipy [35].

At the end we got a table of pictures (nodes); for each node we got its radius as well as position and the list of nodes that we were able to reach starting from there; and another table with edges and their characteristics. Based on this, we derived the data in Table III.

These figures can be compared to typical characteristics found in experiments [27].

The bundles are formed by depletion forces and neighboring filaments will maximize their overlap region; the bundles will be at least as long as the longest filaments, experimentally it is even hard to form super long bundles. A typical length distribution of actin filaments has mean value of about 9–10 μm, which is already rather long, and a range between 10 and 50 μm for bundles. In our model, the length distribution is quite skewed, with 80% edges lengths in the range 10–30 μm and another 7% in the range 30–50 μm.

About bundle sizes, 84% of radii in the model are in the range 1.22–3.42 μm. This can be considered a reasonable estimation and compares well to the experiments [27].

The average number of filaments in bundles is quite difficult to measure experimentally. An estimation based on comparing the fluorescence intensity of a bundle against a single filament yielded a result of 45 ($\pm$25) filaments per bundle [36]. Considering even small bundles having 100 nm radius, we find that they can accommodate more than 100 filaments, considering a radius of 5.4 nm plus 2λ_B. For this reason, the low density model for bundles is probably appropriate, and we decided to not consider possible interactions between actin filaments within the bundles.

As an illustration, in Fig. 2 the white lines drawn on the original image represent the computed edges.

In a realistic experiment, one would have to set a support with electrodes in contact with the network. In a typical configuration, we will consider a grid of 5 × 6 electrodes, for instance, on a thin glass; their diameter is 10 μm and center-to-center distances are 30 μm. We considered two situations: (1) the network is grown in droplets sitting on the glass
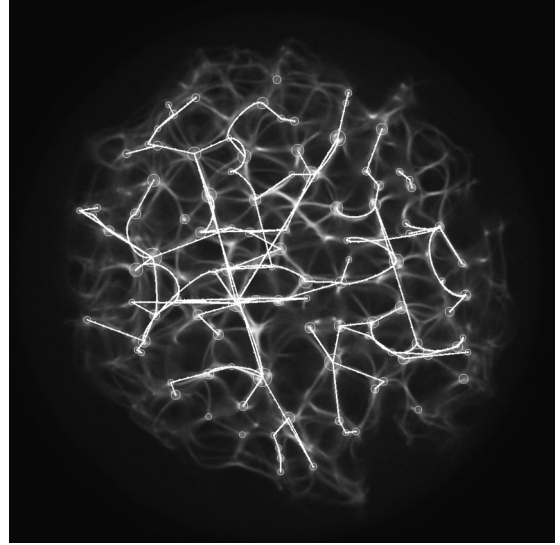

FIG. 2. Two-dimensional centers and edges of a Z slice.

surface, which holds the electrodes. This is actually very close to the experimental setup described in [27,37]. And (2) the array of electrodes is set inside the network, i.e., in the middle of the actin droplet along its vertical axis. This might be the case if the networks were grown around the electrode layer or if it were placed in the network later. Figure 3 is an illustration of the network grown on top of the electrode-containing glass.

The general features of the network are listed in Table III.

V. PRELIMINARY RESULTS

We used the simplest possible form for the input functions F_n, which are constant functions:

$$\text{for } 0 < t < t_1 \; F_n \equiv \begin{cases} 1 & \text{if } n \in N_1, \\ 0 & \text{if } n \in N_0, \\ -1 & \text{if } n \in N_{-1}, \end{cases} \quad (9)$$
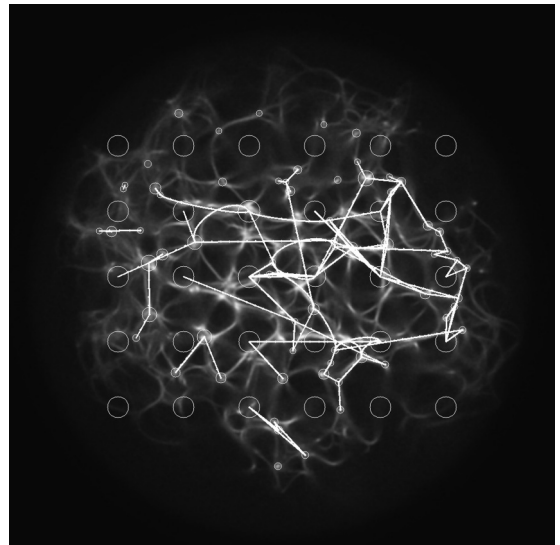

FIG. 3. The grid of electrodes as it appears when the network formed on top of the supporting glass.
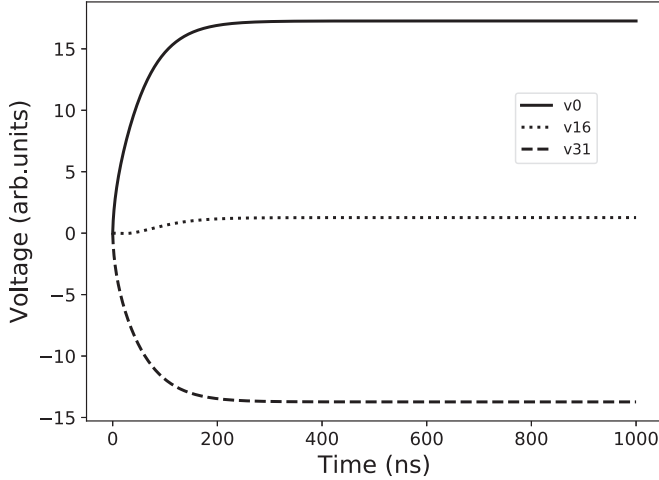
FIG. 4. Evolution of the potential of first, middle, and last elements of an open high density (H.D.) bundle 32 elements long, 450 nm thick. Input was set at 1 and −1 at the first and last elements.

where N_1, N_0, and N_{-1} are three sets of indices and t_1 is the duration of the input stimuli, which can be equal to or less than the whole experiment time.

Numerical integration has been performed for bundles consisting of some tens of elements using various stimuli and electrical values. We considered both open bundles with free extremal elements, and closed ones where every element is connected to two others. Examples can be found in Fig. 4 (high density open bundle) and Fig. 5 (low density closed bundle).

These numerical experiments demonstrate that in all the cases considered, the solutions become constant after a transient time. Moreover, when the inputs are blocked all the solution converge to the same constant value, so that no currents can be detected.

We therefore considered constant stimuli lasting for all the experiment time and searched for constant solutions. Input
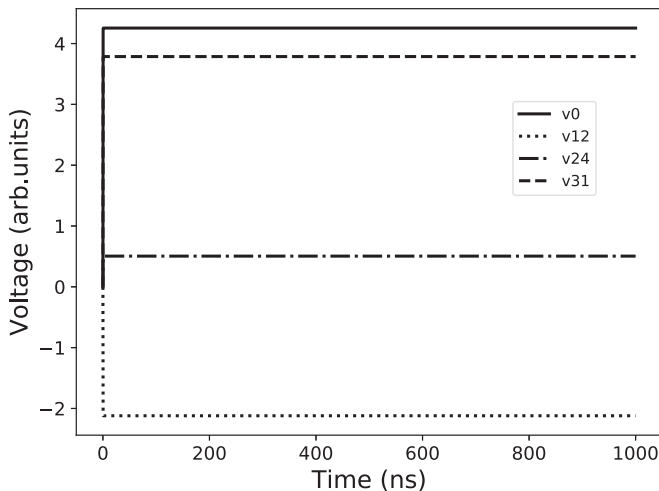

FIG. 5. Evolution of the potential of some elements of a closed low density (L.D.) bundle 32 elements long, made of 50 filaments. Input was set at 1 and −1 at elements with index 0 and 15.

TABLE IV. Number of possible NOT gates.

Run	Thresh. 2	Thresh. 1	Thresh. 0.5
1	8266	8944	8409
2	3688	4660	4682
3	5730	7043	7455

bits are defined as a pair of points of the network, so that a $+1$ potential (in arbitrary units) is applied at one of them and -1 at the other to encode a value 1 of the bit; when no potential is applied, the bit value is zero.

Analogously, we chose pairs of points and measured the difference of their potential to read an output bit. A suitable threshold has been defined to distinguish the 1 and 0 values.

VI. RESULTS

A. Ideal electrodes

In this section we consider ideal electrodes that (1) can be placed in any point on the network surface or inside it and (2) are so small that they would be in contact with one element of a single bundle only. Moreover, we use a slightly idealized network of spherical shape.

1. Boolean gates

We have randomly chosen eight sites in the network and considered them as four pairs to represent four input bits.

Then we applied in turn all the possible input states from (0000) to (1111) and solved the system (8). It reduces to a linear algebraic structure and simplifies finding the values of the potential in the *nodes*. Then we checked, for all the sets of input states that correspond to a logical input, which output bits correspond to the expected results for a gate.

For instance, to find the NOT gates we considered input state sets ((0000),(0001)), ((1000),(1001)) etc.; then we looked for all the output bits that are 1 for the first state and 0 for the second of one of the input sets.

The same procedure was used to find OR, AND, and XOR gates. We used three values for the output threshold: 2, 1, and 0.5.

The results of three runs are shown in Tables IV, V, VI, and VII revealing that once an input position is chosen, it is possible to find a suitable number of edges that behave as output for the main gate types.

2. Time estimates

We also computed the time that the network would need to converge to the constant solutions taking the time into account needed for an element to discharge. As a first estimate, we

TABLE V. Number of possible OR gates.

Run	Thresh. 2	Thresh. 1	Thresh. 0.5
1	4385	8191	12 494
2	6360	8188	11 336
3	5835	8260	11 063

TABLE VI. Number of possible AND gates.

Run	Thresh. 2	Thresh. 1	Thresh. 0.5
1	3600	3562	2577
2	4506	43842	3119
3	4954	5076	3726

used the value R_1C_0, that is the discharge time of a pure RC circuit. Using the parameters for a single filament (or for low density bundles made of independent filaments), we got 2.248×10^{-3} s to travel the 3 843 876 elements of the whole network. Parameters for a high density network, adjusted for the estimated width of each bundle, gave a time of 2.25×10^{-3} s. In both cases, the velocity is of the order of 4.7 m/s, two orders of magnitude larger than the estimate found in [20] with a different model (pure RC), but in the range estimated in [3] using the presented method.

B. Realistic electrodes

In this section we consider electrodes that could be actually available, with their supporting glass. Moreover, we use the real network dimensions (the confocal images are $250 \times 250 \ \mu m^2$ and they are spaced 110 μm in depth).

We considered both the case with the network being on top of the glass holding the electrodes, and the case when the electrodes are placed inside the network, along the middle plane of the confocal image stack.

In the case of the network on top of the glass, we have randomly chosen eight electrodes and considered them as four pairs to represent four input bits.

We applied in turn all the possible input states from (0000) to (1111) and solved the system (8). Then we computed the potential differences for all the pairs of electrodes that were not used as input and applied a suitable threshold to distinguish 0 and 1 bits. The threshold we used was the median of the differences.

As 10 electrodes out of the 18 connected to the network were not used as input, we had 45 potential output bits. We found that, considering all the possible input and output bits, we have 101 NOT gates, 113 OR gates, 46 AND gates, and 13 XOR gates.

It must be noted that the same pair of output electrodes may have been counted many times in these numbers. For instance, the potential difference of electrodes between 46th and 32nd electrode (electrodes in row 4 column 6 and in row 3 column 2), were considered a possible NOT gate for all the cases listed in Table VIII.

In the case of the network with electrodes placed in the interior of the network, we have randomly chosen 12 electrodes and considered them as 6 couples to represent 6 input bits.

TABLE VII. Number of possible XOR gates.

Run	Thresh. 2	Thresh. 1	Thresh. 0.5
1	1543	2155	3749
2	584	986	1799
3	1009	1499	3083

TABLE VIII. Possible NOT with a single edge.

Input state	Output value	NOT on bit
1100	1	4
1101	0	
1010	1	4
1011	0	
1000	1	4
1001	0	
0110	1	4
0111	0	
0100	1	4
0101	0	
0111	0	2
0011	1	
0101	0	2
0001	1	
1011	0	1
0011	1	
1001	0	1
0001	1	

We applied in turn all the possible input states from (000000) to (111111) and solved the system (8). Then we computed the potential differences for all the pairs of electrodes that were not used as input and applied a suitable threshold to distinguish 0 and 1 bits. The threshold we used was the median of the differences.

As 15 electrodes out of the 27 connected to the network were not used as input, we had 105 potential output bits. We found that, considering all the possible input and output bits, we have 1885 NOT gates, 1279 OR gates, 783 AND gates, and 467 XOR gates.

VII. FINITE STATE MACHINE

The actin network implements a mapping from $\{0, 1\}^k$ to $\{0, 1\}^k$, where k is a number of input bits represented by potential difference in pairs of electrodes, as described above. Thus, the network can be considered as an automaton or a finite state machine, $\mathcal{A}_k = \langle \{0, 1\}, C, k, f \rangle$. The behavior of the automaton is governed by the function $f : \{0, 1\}^k \to \{0, 1\}^k$, $k \in \mathbf{Z}_+$. The structure of the mapping f is determined by exact configuration of electrodes $C \in \mathbf{R}^3$ and geometry of the AF bundle network.

The machine $\mathcal{A}_4$ represents the actin network placed onto an array of electrodes. In this case, having at our disposal 45 potential output bits, the number of combinations of 4 of them is 148 995. We therefore limited the study at the output positions that assume a 1 value more than 6 and less than 11 times for the 16 input states. In this way we found 11 output bits and computed the state transitions for the 330 machines that one can obtain choosing 4 out of them, $k = 4$.

The machine $\mathcal{A}_6$ represents the actin network where the array of electrodes is inside the network. In this case, having at our disposal 105 potential output bits, the number of combinations of 6 of them is quite large. We therefore limited the study at the output positions that assume a 1 value 32 times for the 64 input states. In this way we found again 11 output
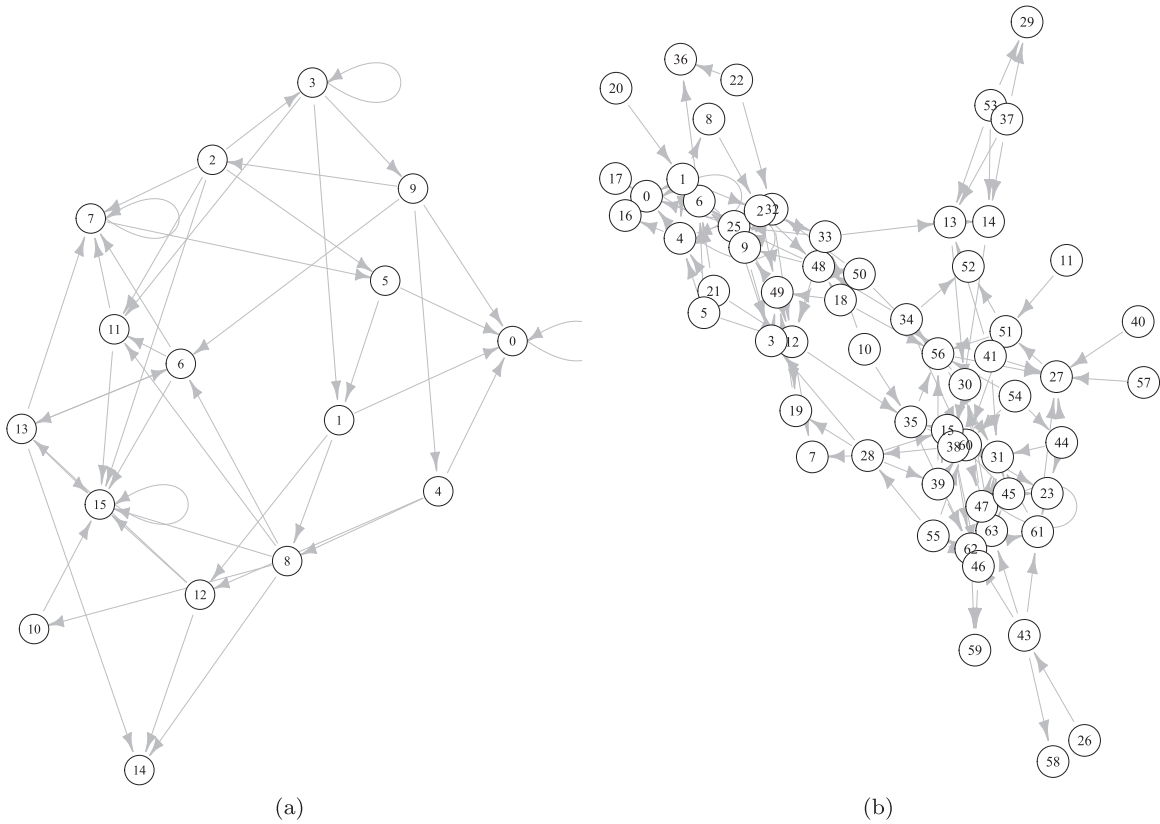
FIG. 6. State transitions graphs for (a) $\mathcal{A}_4$ and (b) $\mathcal{A}_6$, trimming threshold is $\theta = 0.1$. Nodes are labeled by digital representation of 4-bit (a) and 6-bit (b) states.

bits and computed the state transitions for the 462 machines that one can obtain choosing 6 out of them, $k = 6$.

We derived structures of functions f_4 and f_6, governing behavior of automata $\mathcal{A}_4$ and $\mathcal{A}_6$, as follows. There is potentially an infinite number of electrode configurations from $\mathbf{R}^3$. Therefore, we selected 330 and 462 configurations C for machines $\mathcal{A}_4$ and $\mathcal{A}_6$, respectively, and calculated the frequencies of connections of input to output states, obtaining two probabilistic state machines $= \langle \{0, 1\}, p, k, f \rangle$, where $p : \{0, 1\}^{k\{0,1\}} \rightarrow [0, 1]$, the p assigns a probability to each mapping from $\{0, 1\}^k$ to $\{0, 1\}$. Thus, a state transition of $\mathcal{A}_k$ is a directed weight graph, where weight represents a probability of the transition between states of $\mathcal{A}_k$ corresponding to nodes of the graph. The weighted graph can be converted to a nonweighted directed graph by removing all edges with weight less than a given threshold θ. In the following we perform trimming for several thresholds with 0.1 increment.

The graph remains connected for θ till 0.1 (Fig. 6). The graph for $\mathcal{A}_4$ is characterizing for having no unreachable nodes and several absorbing states [Fig. 6(a)] while the graph for $\mathcal{A}_6$ has a number of unreachable nodes (Garden-of-Eden states) and less, than $\mathcal{A}_4$, absorbing states [Fig. 6(b)].

The state transition graph of $\mathcal{A}_6$ becomes disconnected for $\theta = 0.2$ [Fig. 7(b)] and the graph of $\mathcal{A}_4$ remains connected [Fig. 7(a)].

Another way of converting weighted, probabilistic, state transition graphs into nonweighted graphs is by selecting for

each node x a successor y such that the weight of the arc (xy) is the highest among all arcs outgoing from x. These graphs G_4 and G_6 of most likely transitions are shown in Fig. 8. The graph G_4 [Fig. 8(a)] has two disconnected subgraphs, eight Garden-of-Eden states, and two absorbing states corresponding to (1111) and (0000); the graph has no cycles. The graph G_6 has five disconnected subgraphs [Fig. 8(a)]. Two of them have only absorbing states, corresponding to (00000) and (101010), and no cycles. Three of the subgraphs do not have an absorbing state but have cycles: $(111110) \rightarrow (111111) \rightarrow (111110)$, $(001111) \rightarrow (001111) \rightarrow (100110) \rightarrow (111100) \rightarrow (001111)$ and $(000011) \rightarrow (110001) \rightarrow (001001) \rightarrow (000010) \rightarrow (100001) \rightarrow (001100) \rightarrow (000011)$.

VIII. DISCUSSION

By using a physical model of ionic currents on a nonlinear transmission network we demonstrated how a computation of Boolean functions can be implemented on actin networks and what type of distribution of Boolean gates can be obtained. In the model we employed a geometry of the three-dimensional actin bundle network derived from experimental laboratory data. Our results might act as a feasibility study for future experimental laboratory prototypes of cytoskeleton computing devices. We have also derived finite state machines realizable on the actin networks. The importance of the machines is twofold. First, their state transition graphs might act as unique fingerprints of actin networks formed at the different

FIG. 7. State transitions graphs for (a) $\mathcal{A}_4$ and (b) $\mathcal{A}_6$, trimming threshold is $\theta = 0.2$. Nodes are labeled by digital representation of 4-bit (a) and 6-bit (b) states, respectively.

experimental or physiological conditions. Second, the structure of the machines could advance studies in computational power of actin networks in the context of formal language recognition.

We recall that probabilistic finite-state machines are syntactic objects which can model and generate distributions over sets of possible infinite cardinality of strings, sequences, words, phrases, terms, and trees. In particular they are known to recognize uncountably many languages. The interested reader is referred, e.g., to [38,39].

Of course the actin structures described by our model would not immediately be used to build powerful calculating machines like our modern computers. However, our results may serve as a proof of principle that such structures may be able to fulfill rudimentary processing tasks. For example, if computing chips could be build with these structures, they would be completely biodegradable and recycling would not be an issue. This may pave the way for modern, green technologies. Of course all these statements are too far reaching for such a study, which is a basic research approach. Generally, the type of actin networks we used in our experiments are especially suitable for such an initial approach since they form very robust, highly reproducible structures, which remain stable over weeks.

Moreover, we emphasize that understanding the electrical properties of actin networks, or more explicitly of actin bundles and their networks, would provide a broad range of information. In the field of biophysics many different labs

around the world measure electrical properties, especially the impedance, of a cell as a potential readout for pathological transformation, for instance, during cancer development [1]. Different cells do show different impedance results, however, the origin of the difference is still not resolved. Our findings prove that signal transduction depends on the geometry of the system, a principle which ultimately may help to understand the cellular studies.

The following issues could be addressed in the future. We did not consider the currents generated by ions flowing in the liquid medium containing the network, which could produce some amount of noise. The model could be improved in this aspect. We did not account for the fact that differences of electrical potentials along the bundles could give rise to local patterns of ion concentrations, and these, in turn could change the bundle resistance R_1. This could be a retrofit mechanism that we propose to study in future work.

It should also be noted that similar implementations of the model involving MTs instead of AFs are possible with minor modifications. Random arrangements of MTs in buffer solutions have been analyzed experimentally regarding their conductive and capacitive properties [40–42]. It was observed that MTs measurably increase the solution's conductance compared to free tubulin at lower ionic concentrations while the opposite is true at high ionic concentrations. This effect can be explained using the Debye-Hueckel model as due to the formation of a counterionic layer, whose thickness is concentration and temperature dependent according to the
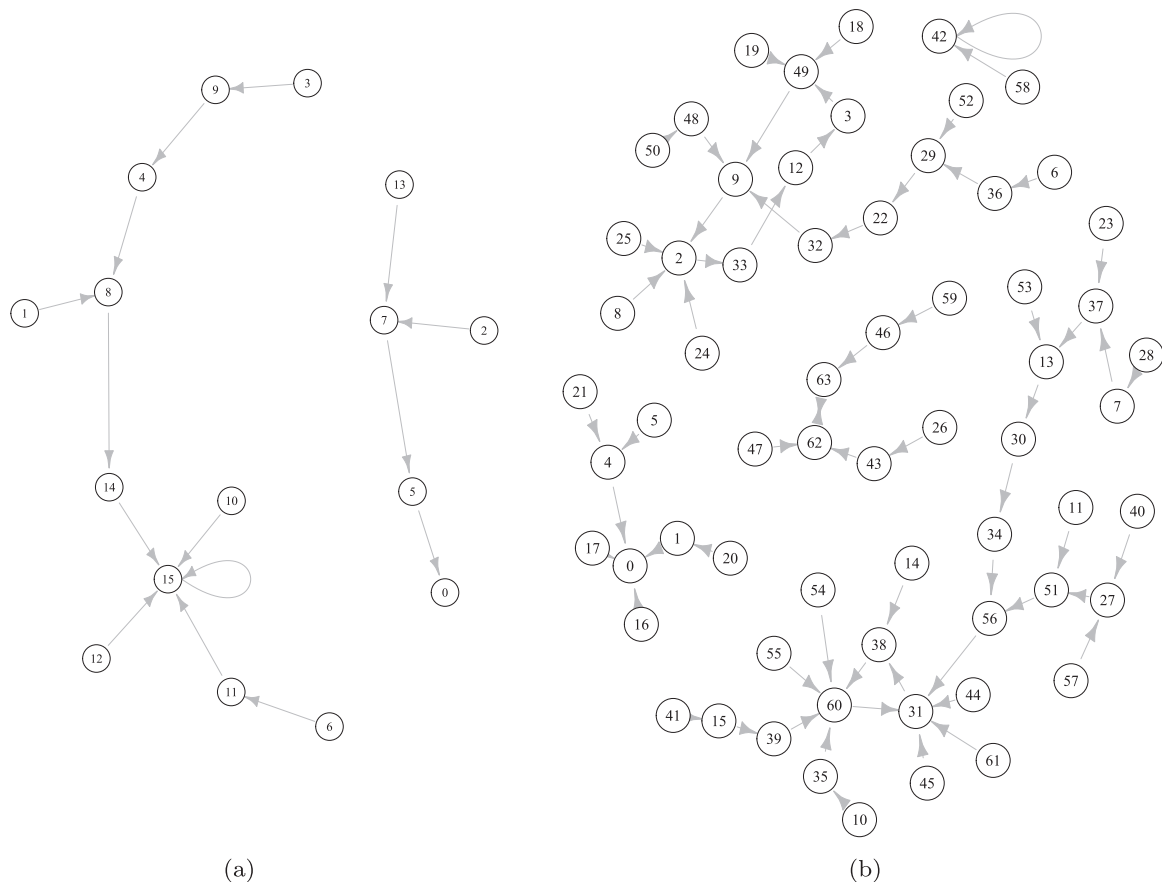
FIG. 8. Graphs representing most likely transitions G_4 (a) and G_6 (b) of $\mathcal{A}_4$ (a) and $\mathcal{A}_6$ (b).

Debye length formula. At high ionic concentrations, MTs act as low-resistance cables while at low ionic concentrations their contribution to impedance is mainly capacitive. At the peak value, the intrinsic conductivity of MTs has been found to be two orders of magnitude greater than that of the buffer solution. On the other hand, at low protein concentration, free tubulin dimers decrease the solution's conductance, and it was modeled as being due to tubulin attracting ionic charges and lowering their mobility. Both tubulin and MTs were found to increase capacitance of buffer solutions, due to their formation of ionic double layers. Consequently, MT networks exhibit fascinating electrical properties, which change as a function of ionic concentration and pH providing an opportunity to additionally control the functional characteristics of the networks assembled from MTs. We intend to derive a complete model based on MT networks in a future study.

[1] F. Huber, J. Schnauß, S. Rönicke, P. Rauch, K. Müller, C. Fütterer, and J. A. Käs, Emergent complexity of the cytoskeleton: From single filaments to tissue, Adv. Phys. **62**, 1 (2013).

[2] A. Priel, J. A. Tuszynski, and H. F. Cantiello, Ionic waves propagation along the dendritic cytoskeleton as a signaling mechanism, Adv. Mol. Cell Biol. **37**, 163 (2006).

[3] J. A. Tuszyński, S. Portet, M. Dixon, C. Luxford, and H. F. Cantiello, Ionic wave propagation along actin filaments, Biophys. J. **86**, 1890 (2004).

[4] M. V. Satarić, D. I. Ilić, N. Ralević, and J. A. Tuszynski, A nonlinear model of ionic wave propagation along microtubules, Eur. Biophys. J. **38**, 637 (2009).

[5] M. V. Satarić, D. Sekulić, and M. Živanov, Solitonic ionic currents along microtubules, J. Comput. Theor. Nanosci. **7**, 2281 (2010).

[6] A. Priel and J. A. Tuszyński, A nonlinear cable-like model of amplified ionic wave propagation along microtubules, Europhys. Lett. **83**, 68004 (2008).

[7] D. L. Sekulić, B. M. Satarić, J. A. Tuszynski, and M. V. Satarić, Nonlinear ionic pulses along microtubules, Eur. Phys. J. E **34**, 49 (2011).

[8] M. V. Satarić and B. M. Satarić, Ionic pulses along cytoskeletal protophilaments, J. Phys. Conf. Ser. **329**, 012009 (2011).

[9] S. R. Hameroff and R. C. Watt, Information processing in microtubules, J. Theor. Biol. **98**, 549 (1982).

[10] S. Hameroff, A. Nip, M. Porter, and J. Tuszynski, Conduction pathways in microtubules, biological quantum computation, and consciousness, Biosystems **64**, 149 (2002).

[11] S. Hagan, S. R. Hameroff, and J. A. Tuszyński, Quantum computation in brain microtubules: Decoherence and biological feasibility, Phys. Rev. E **65**, 061901 (2002).

[12] J. A. Tuszyński, S. Hameroff, M. V. Satarić, B. Trpisova, and M. L. A. Nip, Ferroelectric behavior in microtubule dipole lattices: Implications for information processing, signaling and assembly/disassembly, J. Theor. Biol. **174**, 371 (1995).

[13] J. A. Brown and J. A. Tuszyński, Dipole interactions in axonal microtubules as a mechanism of signal propagation, Phys. Rev. E **56**, 5834 (1997).

[14] M. Cifra, J. Pokorn, D. Havelka, and O. Kučera, Electric field generated by axial longitudinal vibration modes of microtubule, BioSystems **100**, 122 (2010).

[15] A. Adamatzky, J. Tuszynski, J. Pieper, D. V. Nicolau, R. Rinalndi, G. Sirakoulis, V. Erokhin, J. Schnauss, and D. M. Smith, Towards cytoskeleton computers. A proposal, in *From Parallel to Emergent Computing*, edited by A. Adamatzky, S. Akl, and G. Sirakoulis (CRC Group/Taylor & Francis, London, 2019).

[16] S. R. Hameroff and S. Rasmussen, Information processing in microtubules: Biomolecular automata and nanocomputers, in *Molecular Electronics* (Springer, Berlin, 1989), pp. 243–257.

[17] S. Rasmussen, H. Karampurwala, R. Vaidyanath, K. S. Jensen, and S. Hameroff, Computational connectionism within neurons: A model of cytoskeletal automata subserving neural networks, Physica D **42**, 428 (1990).

[18] S. Hameroff and S. Rasmussen, Microtubule automata: Subneural information processing in biological neural networks, in *Theoretical Aspects of Neurocomputing*, Selected Papers from the Symposium on Neural Networks and Neurocomputing (NEURONET '90), edited by M. Novák and E. Pelikán (World Scientific, Singapore, 1990).

[19] A. Priel, J. A. Tuszynski, and H. F. Cantiello, The dendritic cytoskeleton as a computational device: an hypothesis, in *The Emerging Physics of Consciousness* (Springer, Berlin, 2006), pp. 293–325.

[20] J. J. A. Tuszynski, M. V. Sataric, D. L. Sekulic, B. M. Sataric, and S. Zdravkovic, Nonlinear calcium ion waves along actin filaments control active hair-bundle motility, Biosystems **173**, 181 (2018).

[21] S. Siccardi, J. A. Tuszynski, and A. Adamatzky, Boolean gates on actin filaments, Phys. Lett. A **380**, 88 (2016).

[22] J. Schnauß, T. Händler, and J. A. Käs, Semiflexible biopolymers in bundled arrangements, Polymers **8**, 274 (2016).

[23] J. Schnauß, T. Golde, C. Schuldt, B. U. Sebastian Schmidt, M. Glaser, D. Strehle, T. Händler, C. Heussinger, and J. A. Käs, Transition from a Linear to a Harmonic Potential in Collective Dynamics of a Multifilament Actin Bundle, Phys. Rev. Lett. **116**, 108102 (2016).

[24] J. S. Lorenz, J. Schnauß, M. Glaser, M. Sajfutdinow, C. Schuldt, J. A. Käs, and D. M. Smith, Synthetic transient crosslinks program the mechanics of soft, biopolymer-based materials, Adv. Mater. **30**, 1706092 (2018).

[25] A. Adamatzky, F. Huber, and J. Schnauß, Computing on actin bundles network, Sci. Rep. **9**, 15887 (2019).

[26] A. Adamatzky, J. Schnauß, and F. Huber, Actin droplet machine, R. Soc. Open Sci. **6**, 191135 (2019).

[27] F. Huber, D. Strehle, J. Schnauß, and J. Käs, Formation of regularly spaced networks as a general feature of actin bundle condensation by entropic forces, New J. Phys. **17**, 043029 (2015).

[28] Z.-S. Ma, J. Wang, and H. Guo, Weakly nonlinear ac response: Theory and application, Phys. Rev. B **59**, 7575 (1999).

[29] B. Wang, X. Zhao, J. Wang, and H. Guo, Nonlinear quantum capacitance, Appl. Phys. Lett. **74**, 2887 (1999).

[30] T. E. Angelini, H. Liang, W. Wriggers, and G. C. L. Wong, Like-charge attraction between polyelectrolytes induced by counterion charge density waves, Proc. Natl. Acad. Sci. **100**, 8634 (2003).

[31] S. Asakura and F. Oosawa, Interaction between particles suspended in solutions of macromolecules, J. Polym. Sci. **33**, 183 (1958).

[32] S. Asakura and F. Oosawa, On interaction between two bodies immersed in a solution of macromolecules, J. Chem. Phys. **22**, 1255 (1954).

[33] M. Glaser, J. Schnauß, T. Tschirner, B. U. Sebastian Schmidt, M. Moebius-Winkler, J. A. Käs, and D. M. Smith, Self-assembly of hierarchically ordered structures in DNA nanotube systems, New J. Phys. **18**, 055001 (2016).

[34] J. D. Hunter, Matplotlib: A 2D graphics environment, Comput. Sci. Eng. **9**, 90 (2007).

[35] P. Virtanen, R. Gommers, T. E. Oliphant, M. Haberland, T. Reddy, D. Cournapeau, E. Burovski, P. Peterson, W. Weckesser, J. Bright, S. J. van der Walt, M. Brett, J. Wilson, K. J. Millman, N. Mayorov, A. R. J. Nelson, E. Jones, R. Kern, E. Larson, C. J. Carey, İ. Polat, Y. Feng, E. W. Moore, J. VanderPlas, D. Laxalde, J. Perktold, R. Cimrman, I. Henriksen, E. A. Quintero, C. R. Harris, A. M. Archibald, A. H. Ribeiro, F. Pedregosa, P. van Mulbregt, and SciPy 1.0 Contributors, SciPy 1.0–Fundamental algorithms for scientific computing in Python, Nature Methods **17**, 261 (2020).

[36] D. Strehle, J. Schnauß, C. Heussinger, J. Alvarado, M. Bathe, J. A. Käs, and B. Gentry, Transiently crosslinked F-actin bundles, Eur. Biophys. J. **40**, 93 (2011).

[37] F. Huber, D. Strehle, and J. Käs, Counterion-induced formation of regular actin bundle networks, Soft Matter **8**, 931 (2012).

[38] M. O. Rabin, Probabilistic automata, Inform. Control **6**, 230 (1963).

[39] E. Vidal, F. Thollard, C. de la Higuera, F. Casacuberta, and R. Carrasco, Probabilistic finite-state machines—Part I, IEEE Trans. Pattern Analy. Machine Intel. **27**, 1013 (2005).

[40] A. Pratyaksh Kalra, P. Kar, J. Preto, V. Rezania, A. Dogariu, J. D. Lewis, J. Tuszynski, and K. Shankar, Behavior of α, β tubulin in DMSO-containing electrolytes, Nanoscale Adv. **1**, 3364 (2019).

[41] J. R. Guzman-Sepulveda, Ruitao Wu, A. P. Kalra, M. Aminpour, J. A. Tuszynski, and A. Dogariu, Tubulin polarizability in aqueous suspensions, ACS Omega **4**, 9144 (2019).

[42] I. B. Santelices, D. E. Friesen, C. Bell, C. M. Hough, J. Xiao, A. Kalra, P. Kar, H. Freedman, V. Rezania, J. D. Lewis *et al.*, Response to alternating electric fields of tubulin dimers and microtubule ensembles in electrolytic solutions, Sci. Rep. **7**, 9594 (2017).